

REPORT DOCUMENTATION PAGE

Form Approved
OMB No. 0704-0188

Public reporting burden for this collection of information is estimated to average 1 hour per response, including the time for reviewing instructions, searching existing data sources, gathering and maintaining the data needed, and completing and reviewing this collection of information. Send comments regarding this burden estimate or any other aspect of this collection of information, including suggestions for reducing this burden to Department of Defense, Washington Headquarters Services, Directorate for Information Operations and Reports (0704-0188), 1215 Jefferson Davis Highway, Suite 1204, Arlington, VA 22202-4302. Respondents should be aware that notwithstanding any other provision of law, no person shall be subject to any penalty for failing to comply with a collection of information if it does not display a currently valid OMB control number. **PLEASE DO NOT RETURN YOUR FORM TO THE ABOVE ADDRESS.**

1. REPORT DATE (DD-MM-YYYY) 09-30-2013		2. REPORT TYPE Final technical		3. DATES COVERED (From - To) May 2012 - Jun 2013	
4. TITLE AND SUBTITLE Nanofluidic LaB-ON-Chip Technology for DNA Identification				5a. CONTRACT NUMBER	
				5b. GRANT NUMBER W9132T-12-2-0023	
				5c. PROGRAM ELEMENT NUMBER	
6. AUTHOR(S) Sumita Pennathur				5d. PROJECT NUMBER	
				5e. TASK NUMBER	
				5f. WORK UNIT NUMBER	
7. PERFORMING ORGANIZATION NAME(S) AND ADDRESS(ES) Office of Research University of California 3227 Cheadle Hall, 3rd floor Santa Barbara, CA 93106-2050				8. PERFORMING ORGANIZATION REPORT NUMBER	
9. SPONSORING / MONITORING AGENCY NAME(S) AND ADDRESS(ES) ERDC-CERL ATTN: CECER-CN-E P.O. Box 9005 Champaign, IL 61826-9005				10. SPONSOR/MONITOR'S ACRONYM(S) ERDC-CERL	
				11. SPONSOR/MONITOR'S REPORT NUMBER(S)	
12. DISTRIBUTION / AVAILABILITY STATEMENT Publicly available.					
13. SUPPLEMENTARY NOTES					
14. ABSTRACT In this project we have investigated the potential of nanofluidic lab-on-chip technology to be used as platforms for free-flow separation, concentration, and identification of biomolecules. Specifically, the goals of this project have been to: 1) demonstrate Field Amplified Sample Stacking (FASS) for specific DNA samples, and 2) demonstrate identification of target single stranded DNA (ssDNA) from a complex mixture of DNA, containing strands of different composition and size. We have achieved both goals and, in some cases, expanded the investigation from the original tasks. The results of our studies, elaborated in the following sections, suggest that lab-on-chip nanofluidic platforms may enable rapid and inexpensive, characterization and analysis of DNA biomarkers. Advantages include overall ease of operation of the device, which does not require loading of gels as sieving matrices; inexpensive analysis, as the only reagents required are water-based buffers; fast identification, since sample signatures can be produced in the order of less than a minute. Findings from this work have resulted in peer-reviewed publications (one conference and one journal paper). Potential target applications of our identification platform include analysis of DNA biomarkers for environmental pollutants or early disease diagnosis; analysis of mitochondrial DNA for forensic identification; investigation of protein kinetics.					
15. SUBJECT TERMS DNA separations, nanofluidics, microfluidic capillary electrophoresis (MCE), electrophoretic mobility, FASS, DNA concentration					
16. SECURITY CLASSIFICATION OF:			17. LIMITATION OF ABSTRACT UU	18. NUMBER OF PAGES	19a. NAME OF RESPONSIBLE PERSON Sumita Pennathur
a. REPORT UU	b. ABSTRACT UU	c. THIS PAGE UU			19b. TELEPHONE NUMBER (include area code) (805) 893-5510

Discussion of Final Results

AIM 1: Demonstrate FASS for specific DNA samples, optimizing for buffer concentration and pH, to determine the largest DNA concentration possible in the shortest time.

Nanofluidic technology is gaining popularity for bioanalytical applications due to advances in both nanofabrication and design. One major obstacle in the widespread adoption of such technology for bioanalytical systems is efficient detection of samples due to the inherently low analyte concentrations present in such systems. This problem is exacerbated by the push for electronic detection, which requires an even higher sensor-local sample concentration than optical detection. We have preliminary results showing the potential of FASS as an effective pre-concentration mechanism at the nanoscale [1]. However, before this project we had not explored the case of samples consisting of complex mixtures of DNA. Using FASS would allow for obtaining an on-board concentration method that eliminates PCR amplification and overcomes the related drawbacks that may lead to unreliable analysis results, and prevent absolute quantification of analytes.

A.1 Chemicals and reagents

For all experiments, we used potassium phosphate buffer at pH~7.2, obtained by monobasic and dibasic sodium phosphate (Sigma Aldrich, Inc.) in the appropriate ratios, dissolved in deionized water (Millipore, Inc. pH 7.5). Stock solution of 200 mM was prepared using de-ionized filtered water at 18 MΩ/cm provided by a Millipore Milli-Q Gradient filtration system. The stock solution was then diluted to concentrations of 0.5, 1.0, 2.5, 5.0, 10.0, and 25 mM and seeded with 10 μM sodium fluorescein (Sigma Aldrich, Inc.). The pH and conductivity were then measured (Oakton pH and conductivity meter) and the solution was filtered with 0.2 μm polytetrafluoroethylene syringe filter.

A.1 DNA samples

Fluorescently labeled (FAM tag) DNA oligomers (10, 20, and 50 bases long) were purchased with standard desalting and additional HPLC purification for the 50 base strands, from Integrated DNA Technologies, Inc.

A.1 Experimental setup

The experimental setup is diagramed in Fig. 1. The motion and spatial distribution of the sodium fluorescein was imaged using an inverted epifluorescent microscope (Olympus IX70) fitted with a 60/ 1.00 NA (NA denotes numerical aperture) water objective lens (Olympus, Inc.). Illumination was provided from a 200 W Hg-arc lamp filtered both before and after the sample using interference filters and a dichroic mirror specific to the peak fluorescein absorption and emission wavelengths of 485 and 535 nm, respectively. A ProScan H117 automated stage with a resolution of 0.1 μm was used to monitor the development of the sample ions as they propagate down the East channel. We applied voltages to each well of the nanofluidic channel through platinum electrodes controlled by a multichannel high voltage sequencer (HVS448-6000D, Labsmith, Inc.). A preprogrammed sequence of voltages established the desired fields for flushing, sample loading, gating, and injection/separation estimated using finite element simulations (Comsol, Inc.). We acquired intensity data using a back illuminated and intensified EMCCD camera (Ixon+, Andor Co.) with a 512x512 pixel array and 16-bit digitization. Images

were corrected using MATLAB by subtracting a background image from the raw data and normalizing by the difference between the flatfield and background image following [23].

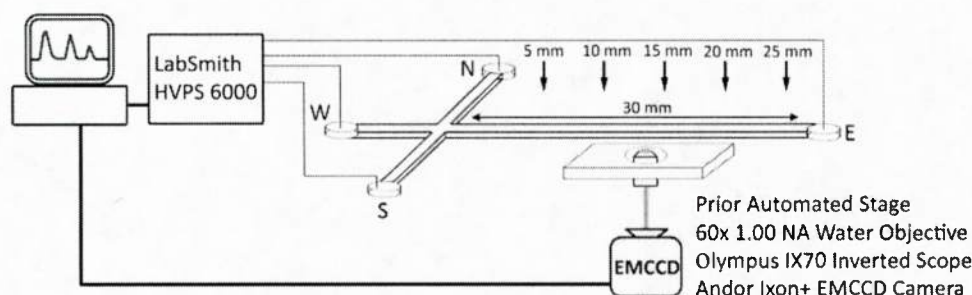


Figure 1: Diagram of the experimental setup. A Prior automated stage (ProScan H117) allowed for real-time observation of the sample as it passed through the detection points of 5, 10, 15, 20, or 25 mm from the intersection.

The interface between high- and lowconductivity buffer regions was generated with potassium phosphate buffer solution, driving the lower conductivity buffer containing the sample from the North to the South well, and the higher conductivity buffer from the West and the East to the South well (Fig. 2, step a). Once a conductivity interface was established, a gating method was necessary to inject enough low-conductivity buffers into the channel to allow for fluorescein to enter the East channel (Fig. 2, step b). Once enough fluorescein entered the East channel, injection voltages were used to propagate the plug down the channel (Fig. 2, step c).

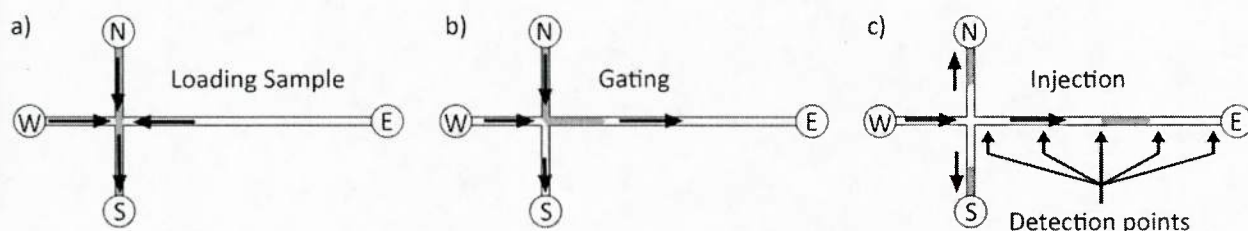


Figure 2: Schematic of sample injection sequence with flow direction denoted with arrows and the low-conductivity sample region is denoted by the shaded area. (a) First, the low-conductivity sample is loaded from the North well to the South well. In this step, high-conductivity buffer is flowing from both the East and West wells toward the South well. (b) Next, gating is performed for several seconds in order to inject a long plug of low-conductivity containing the fluorescent sample. Low-conductivity fluid and sample ions enter the East channel from the North well. (c) Finally, the sample is injected by switching to the injection voltages. Here, high conductivity buffer flows from the West to the East channel, closing off the introduction of sample from the North well and allowing for the sample to propagate as a plug down the channel.

A.1 Experimental Results

Our first experiments served as control and were performed with fluorescein, confirming that at the nanoscale FASS depends on a number of parameters, such as channel height (Figure 3), electrolyte concentration (Figure 4), electric field, gating time, etc.

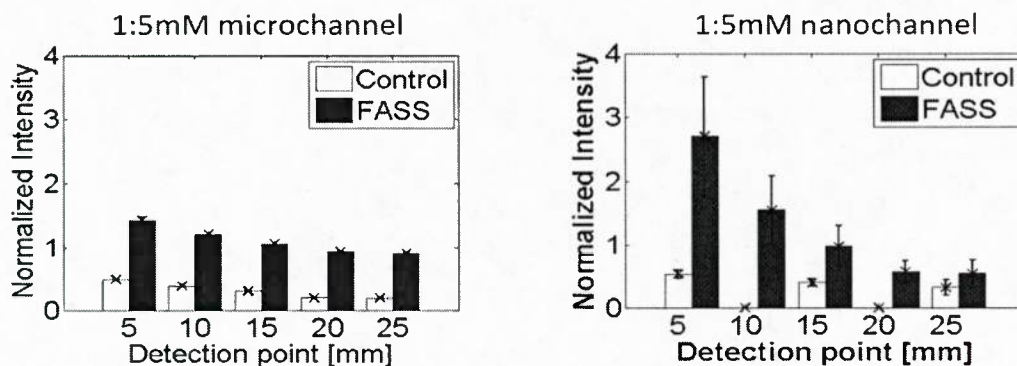


Figure 3: Comparison of FASS concentration enhancement in $1\mu\text{m}$ and 250nm channels. The analyte is $10\mu\text{M}$ fluorescein in $1:10\text{mM}$ phosphate buffer. Note that enhancement in nanochannels can be much larger than in microchannels (up to two orders of magnitude [1]).

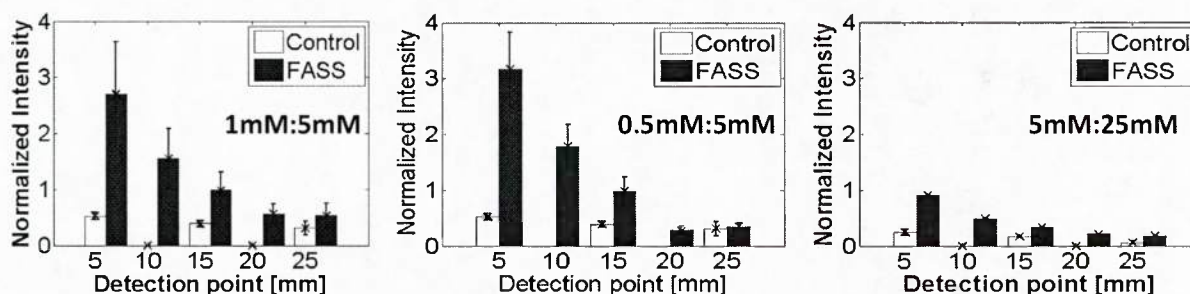
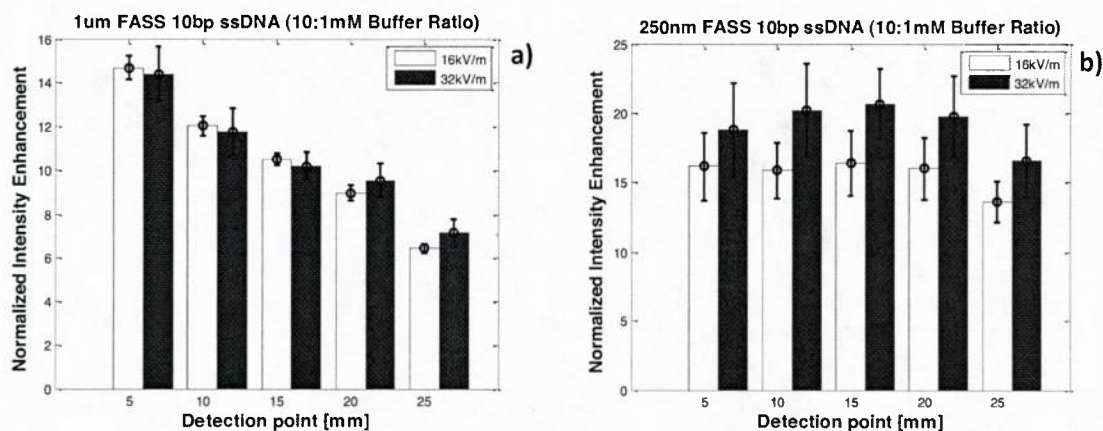


Figure 4: Study of FASS dependence on buffer concentration at the nanoscale in same experimental conditions as in Figure 1. Note that, while in $1\mu\text{m}$ channels the enhancement is roughly constant with concentration ratio, in 250nm channels enhancement strongly depends on background salt concentration: the lower the concentration (e.g., larger EDL), the higher the enhancement.

A qualitatively similar behavior was observed in experiments with DNA samples (10bp ssDNA), as shown in Figure 5, in terms of dependence on buffer concentration, channel size and gating time.



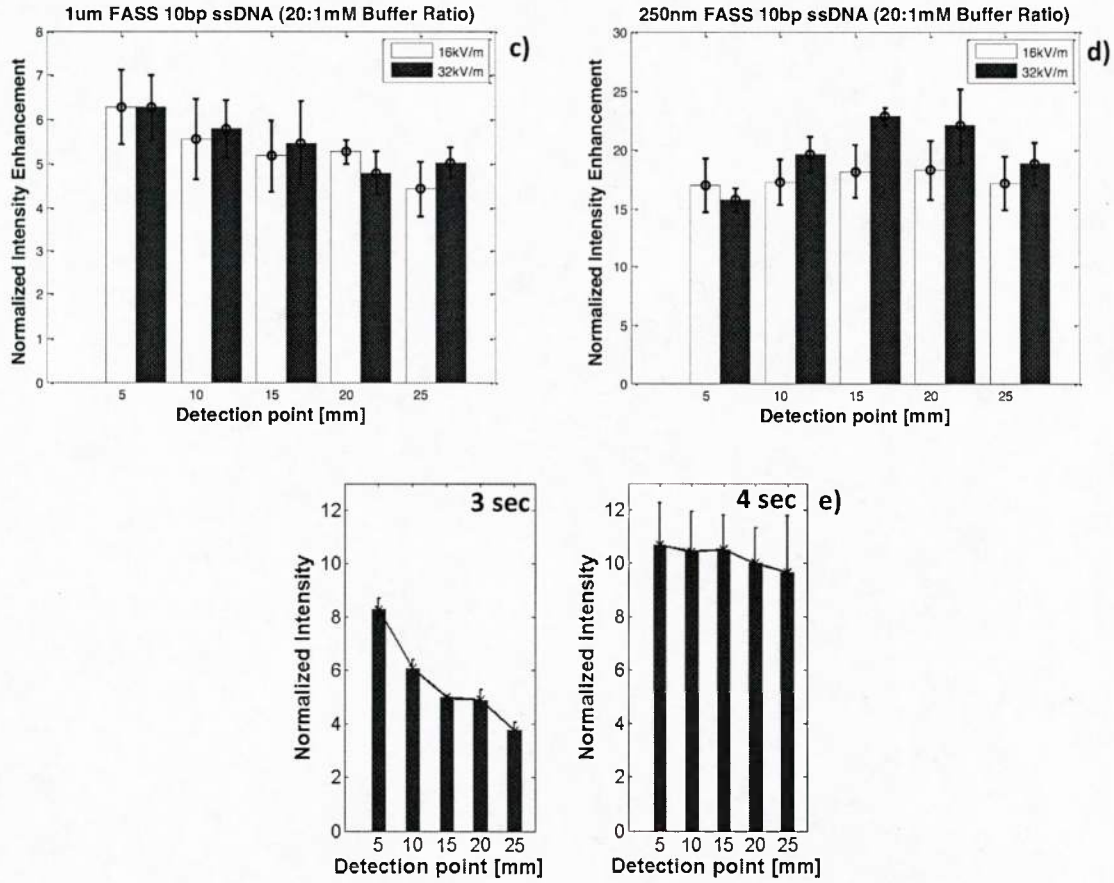


Figure 5: DNA FASS experiments in 1 μm (a-c) and 250nm (b-d-e) channels and different buffer conditions: (a-b) 10:1mM, (c-d) 20:1mM; (e) different gating times in 10:1mM buffer. DNA is 10bp ss, as described in materials section. Error bars represent one standard deviation.

We have observed that, for DNA injections, the gating time was a more critical parameter than fluorescein, in terms of obtaining consistent sample plugs. The inconsistency results in a different amount of sample entering the injection channel, with an obvious impact on the maximum obtainable concentration enhancement. In order to better understand the origin of this phenomenon and optimize injections, we have developed a COMSOL model, consisting of three systems of coupled equations: 1) the mass transport equation,

$$\delta_{ts} \frac{\partial c_i}{\partial t} + \nabla \cdot (-D \nabla c_i - z_i u_{mi} F c_i \nabla V) + \mathbf{u} \cdot \nabla c_i = 0$$

describing the transport of (two) dilute species, c_i , with electromigration and convection terms: c_1 which models the buffer concentration throughout the channel, and c_2 which represents a charged species (e.g., DNA).

2) Gauss law, which describes the electric currents

$$-\nabla \cdot (\epsilon \nabla V) = 0$$

and, thus, governs the electric potential in a conductive media, which we couple to the buffer

concentration to simulate conductivity differences between buffers of different concentration.

3) the continuity and Navier-Stokes equations

$$\nabla \cdot \mathbf{u} = 0$$

$$\nabla \cdot [-p\mathbf{I} + \eta(\nabla \mathbf{u} + (\nabla \mathbf{u})^T)] = 0$$

which govern fluid flow within the channel with electroosmotic flow boundary conditions:

$$\mathbf{u} = \mu_{EO} E_t$$

which creates wall velocity boundary conditions equal to the electroosmotic mobility of the channel. This is coupled to the local electric field from the electric currents module, as well as a zeta potential, which is dependent on the local buffer concentration.

Figure 6 shows a parametric study of the time it takes for fluorescein to enter the injection channel for different buffer concentration ratios. We note that, given an electric field, for increasing buffer ratios, the time fluorescein takes to “enter” the channel (reach a location few microns from the intersection) during gating is longer. During this time, unstable fluid behavior at the intersection prevents fluorescein from entering. The dashed line, t_2 , describes the time for the transient unstable behavior to disappear, and a steady state behavior to emerge.

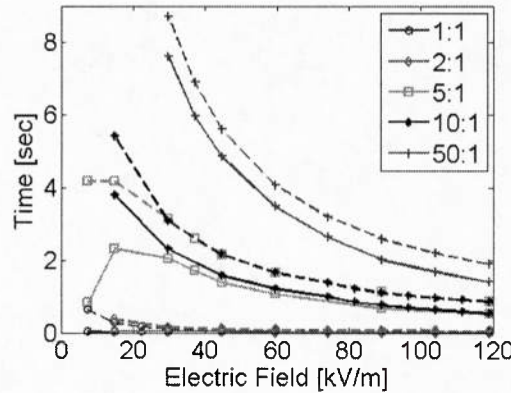


Figure 6: Experimental study of instabilities in FASS for different buffer concentration ratios: 1:1mM (blue – control), 2:1mM (green), 5:1mM (red), 10:1mM (black), and 50:1mM (purple). In all cases, the solid line represents the time t_1 when the sample first enters the east (injection) channel, while the dashed line represents the time t_2 when sample reaches the end of the field of view on the east channel.

In particular, at lower buffer ratios, the sample is let in right away (Figure 7 a-b). At higher buffer ratios, sample is “concentrated” right at the junction before actually entering the injection channel (Figure 7 d). The 5:1 ratio seems to be the “middle” case (Figure 7 c): after gating, sample is let into the injection channel (data not shown), then it is retracted back at the junction where it focuses. The same figure shows the very good qualitative agreement obtained by our numerical simulation.

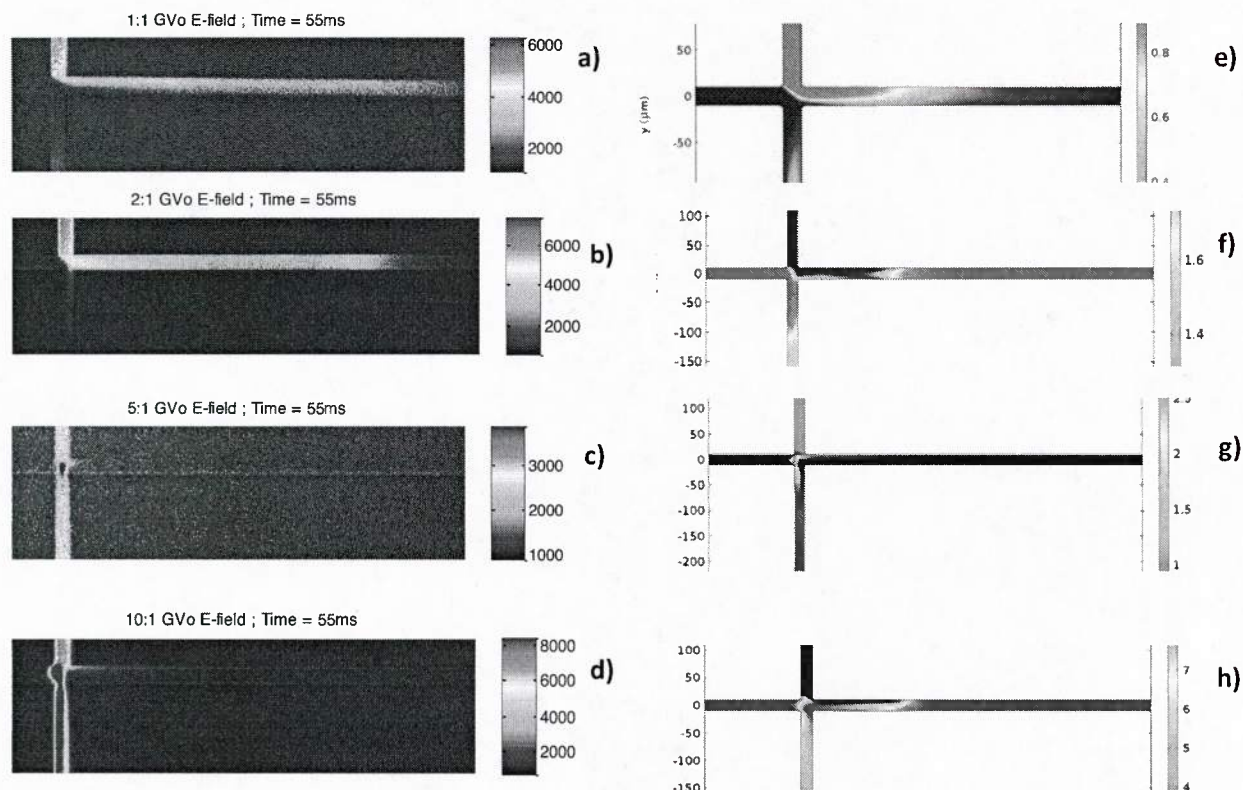


Figure 7: False color images of injection experiments (a-d) and numerical simulations (e-h) for different buffer ratios, and same electric field ($GVo = 120\text{kV/m}$).

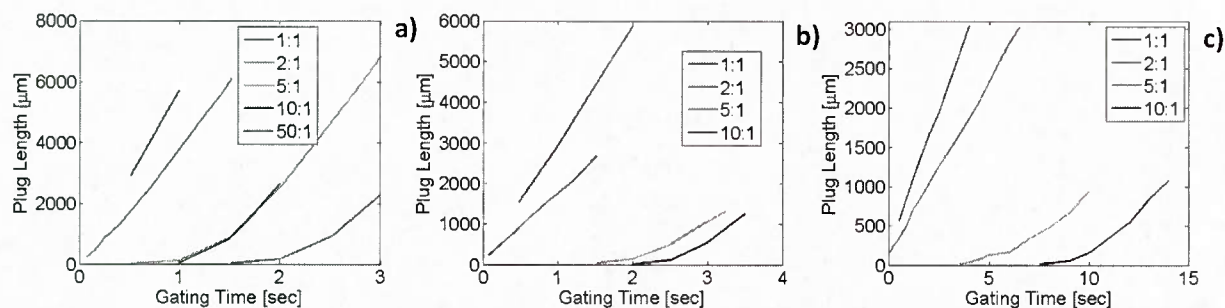


Figure 8: Experimental results showing plug length as a function of buffer concentration for different electric fields: 1) 120kV/m, b) 60kV/m, and c) 15kV/m.

Figure 8 shows experimental data relating plug length to electric field strength, for different buffer concentration ratios. As expected, for lower electric fields and gating times, the sample plugs are shorter. However, we notice the nonlinear behavior for higher buffer concentration ratios, which indicates unstable fluid behavior at the intersection. These flow instabilities prevent fluorescein from entering the channel, resulting in lower amount of sample injected and reduced concentration enhancement. These and other experimental data will be used to improve the model so that it can be used to predict future experiments.

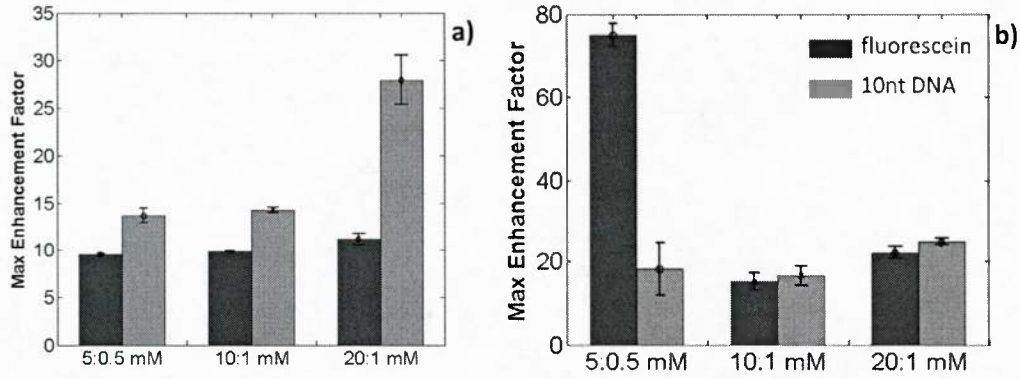


Figure 9: Concentration enhancement for DNA (red) and fluorescein (blue) in: a) 1μm and b) 250nm channels for different buffer concentration ratios.

Figure 9 presents FASS experiments results for fluorescein (blue) and DNA (red) in 1μm and 250nm channels, for different buffer concentration ratios. For DNA and fluorescein in the microchannel case (Fig. 9a), the 10:1 and 5:0.5mM cases yield approximately the same enhancement, equal to the conductivity ratio, although the DNA values are consistently higher. However, for the 20:1mM case, DNA FASS results in a much higher enhancement, which we postulate might be due to the higher negative charge of DNA. In fact, from [1] we know that also in microchannels the maximum enhancement non-linearly depends not only on the EDL thickness, but also on the analyte charge (see Fig. 10 [1], reported below for completeness). Moreover, the transition to the exponential growth region in enhancement strongly depends on the charge of the analyte. Taking the DNA electrophoretic mobility $\mu_{EP} = -3.9e^{-8} [m^2/Vs]$ and diffusivity $D = 2e^{-10} [m^2/s]$, we can roughly estimate the charge number of a 10nt DNA to be $z = \sim 3$: preliminary calculations, using [1], predict a behavior for consistent with measured data (Fig. 9a).

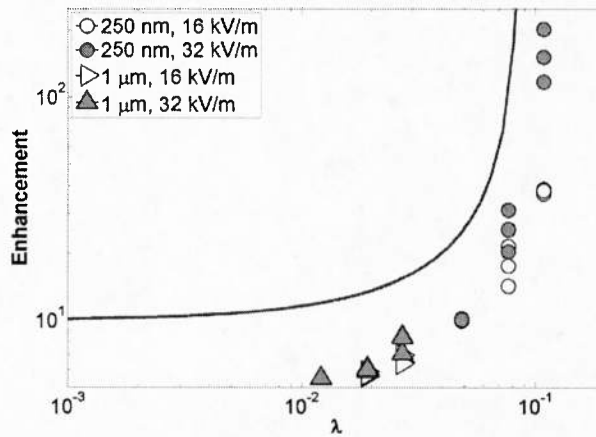


Figure 10 [1]: Maximum theoretical concentration enhancement ratio as a function of Debye length for a 5 mm long plug in a 30 mm straight channel, plotted along with experimental data. In this figure the Debye length is defined for the low-conductivity region and the conductivity ratio is 10 to 1. For this calculation, the concentrations are held fixed at 1 and 10 mM and the channel height is varied. The 250 nm data are shown as circles and the 1 μm channel data are shown as triangles. The experimental data are below the theoretical maximum due to diffusion and other inaccuracies associated with gating and plug length, however the trend is in good agreement with the data. The open shapes are the lower electric field (16 kV/m) and the filled points are for the higher electric fields (32 kV/m).

Regarding the 250nm channels (Fig. 9b), fluorescein data shows the expected behavior, consistent with past results, concentration enhancement is much lower than expected. To understand enhancement limits in 250nm channels, we started by performing experiments with different gating times: since the concentration enhancement depends on amount injected (which will be different at different buffer ratios), are we injecting enough DNA? Or are electrostatic interactions between DNA strands resulting in less analyte being injected?

At first, we recorded and measured the shape and area under the electropherograms at different observation points, to see the progress of analyte stacking. To our surprise (Figure 11), we found that, instead of remaining constant (conservation of mass), the area under the electropherograms was increasing at later observation points. Possible explanations for such behavior are: 1) the quantum efficiency of the FAM dye, which is pH dependent, might cause an increase in brightness as the DNA enters the high conductivity region; 2) while traveling towards the East channel, the sample plug slows down, thus resulting in peak broadening and an apparent larger area.

A new sample batch consisting of DNA tagged with Alexa 448 has been ordered and will be used to continue this investigation after the end of this project. Preliminary measurements of plug speed within 250nm channels do not show any appreciable difference (i.e., slowing down) of DNA compared to fluorescein and compared to what was expected based on our model [1]. More detailed studies are needed to understand the origin of this observed phenomenon.

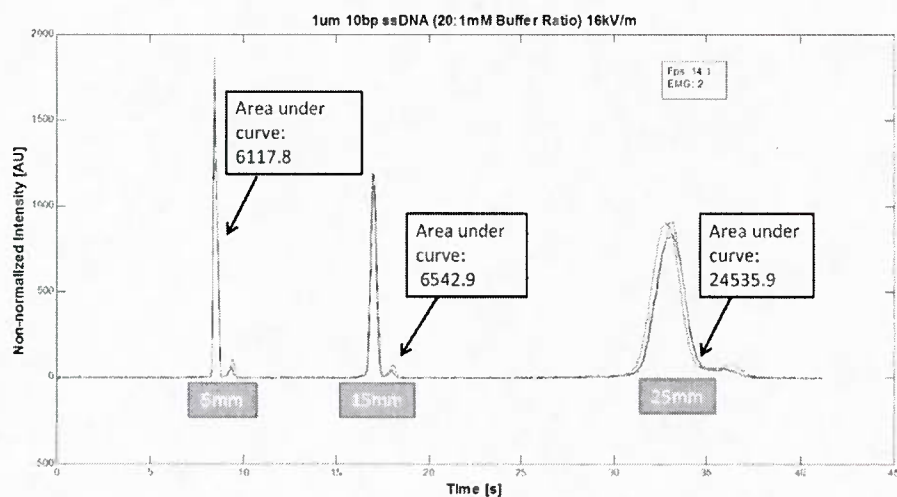


Figure 11: Example of FASS DNA (10nt ssDNA, 20:1mM buffer, 16kV electric field injection) electropherograms collected at different observation points. Notice how the area under each curve, instead of remaining approximately constant, increases with time.

A.1 Conclusions

We have demonstrated that FASS is a viable technique to obtain on-board concentration enhancement of DNA, in both micro and nanochannels. As part of this work, we have also developed a COMSOL prototype model that will allow for studying the instability behavior during injection: such model will prove useful in tuning injection parameters (such as electric fields as a function of buffer concentrations) to obtain repeatable and efficient injections.

Our experiments showed that DNA does not behave like fluorescein and that, therefore, the Matlab model we had previously developed needs to be modified. The origin of the discrepancy in behavior are not yet clear, and further experiments are needed.

AIM 2: Demonstrate identification of target(s) ssDNA from a complex mixture of DNA, containing strands of different composition and size.

We started our investigation by proving that, in nanofluidic channels, different ssDNA could be separated from each other and from the respective dsDNA obtained by hybridization with the corresponding complement (Figure 12 a-b and Figure 14). Figure 12 e) also shows that nanoscale injections can yield information on sample concentration, which is proportional to the area under the peak on the corresponding electropherogram. However, in analyzing the data, we found that in addition to the expected changes in mobility with buffer ionic strength and channel size, the relative changes in mobility between ss and dsDNA become more pronounced as channel size decreases (see Figure 12 e), and that while confinement seems to dominate mobility for ssDNA, dsDNA seem to be more affected by changes in EDL. These results posed fundamental questions on the dynamics of short DNA strands in micro and nano-confinements, which a survey of published literature could not answer. In fact, although there has been significant progress in the experimental characterization of micro and nanofluidic bioanalytical platforms [5–8], the precise mechanism involved with separations of biomolecules at the micro and nanoscale is not fully understood. This is due in part to the nature of biomolecules, which can have complex interactions with each other, as well as with their environment.

To investigate the behavior of short-stranded DNA in micro and nano confinements, we have performed a parametric experimental study on the transport and separation behavior of ss- and dsDNA (10, 20, and 50 bases long), under electrokinetic flows in micro- and nanochannels. We hypothesize that several factors impact electrophoretic mobility: (i) hybridization interactions, (ii) salt-dependent electric double layer (EDL) changes around the DNA, which alter the size/conformation, (iii) differences in drag due to length dependent conformational differences, (iv) hydrodynamic confinement effects due to decreased channel size, and (v) electrostatic repulsion from the walls. These factors have been studied using both analytical and experimental observations towards the optimization of an effective platform for short DNA separation and identification.

A.2 Chemicals and reagents:

Buffered solutions consisted of a 3:17 ratio of monobasic and dibasic sodium phosphate, dissolved in deionized water (Millipore, Inc. pH 7.5) at 10 mM concentration (1.5 mM monosodium phosphate, 8.5 mM disodium phosphate). Buffer ionic strength was varied by the addition of NaCl in concentrations from 5 to 50 mM. All solutions were filtered with 200 nm pore syringe filters (Nalgene, Rochester, NY) prior to use.

A.2 DNA samples:

DNA oligomers (10, 20, 50 nt long) were purchased with standard desalting and additional HPLC purification for the 50 base strands, from Integrated DNA Technologies, Inc. Sequences were designed to be a repetition of the same basic 10 nucleotide “unit” (5'-AA GAG GAG GG - 3'), so that changes in electrophoretic mobility could be attributed to differences in length dependent conformations rather than differences due to sequence or self-complementarity. For

each sequence, we use both a fluorescently labeled, 5' modified (6-FAM) strand and its untagged complement.

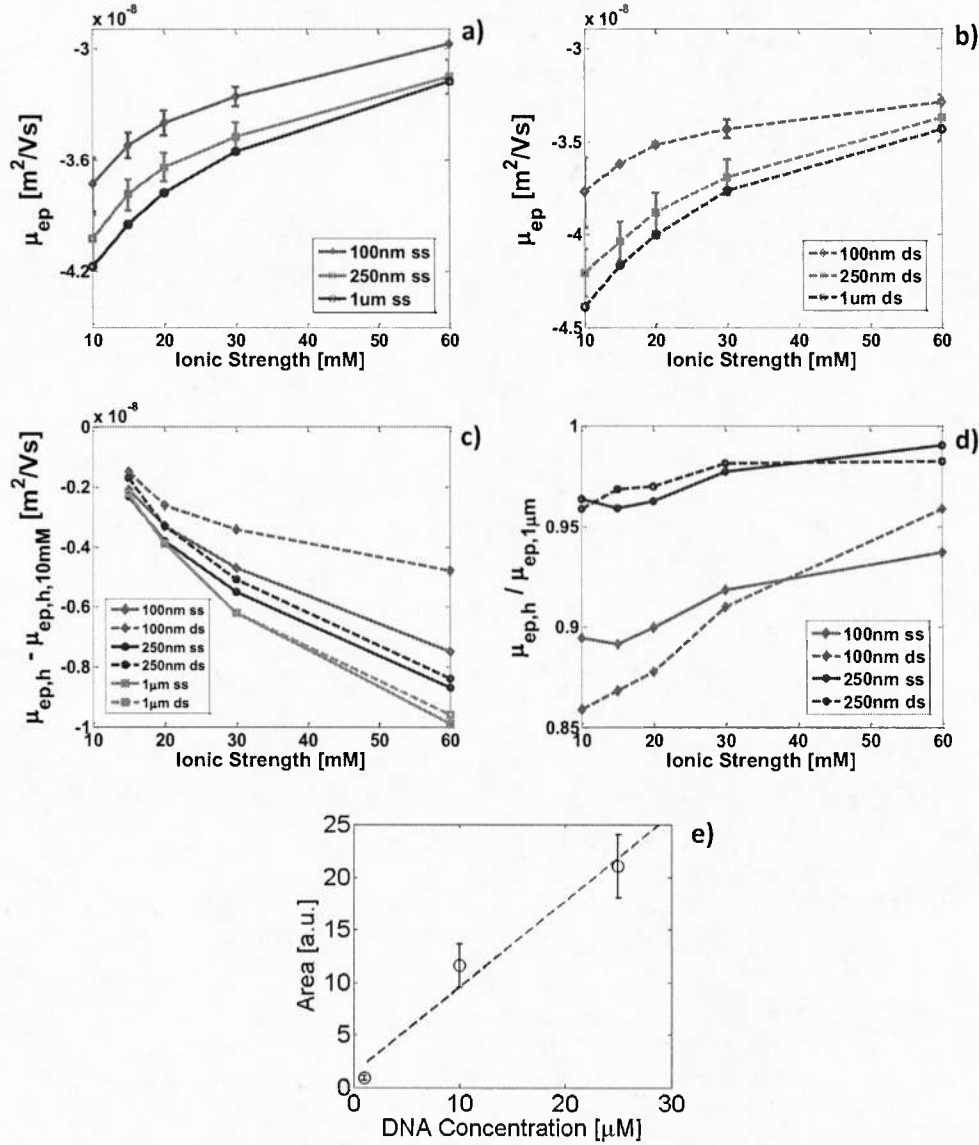


Figure 12: a) and b) Electrophoretic mobility measurements of, respectively, 10 ss- and dsDNA measured in a 1 μm (blue trace), 250nm (red trace) and 100 nm (green trace) deep channels at different ionic strengths. Error bars correspond to the standard deviation of all trials for a given experiment; c) same data but normalized, for each channel depth, by subtracting the corresponding mobility value at 10mM ionic strength; d) same data but normalized by dividing the mobility values at each ionic strength by the corresponding value for 1 μm deep channel; e) quantification of DNA concentration (50 nt ssDNA in 10mM phosphate buffer) in a nanochannel.

A.2 Microfluidic device and setup:

Microchannel devices were designed and custom fabricated in borosilicate wafers using conventional MEMS processing techniques (Dolomite Ltd, UK). The devices consist of a simple cross channel geometry, either 100 nm deep and 7 μm wide, or 1 μm deep and 9 μm wide, with four inlet/outlet ports (labeled N, S, E, W, shown in Figure 13). Electrical potentials were applied

at these wells using platinum electrodes (Omega Eng. Inc., Stamford, CT), connected to a high voltage power supply (LabSmith HVS448). The pre-programmed voltage scheme for sample loading and injection was designed following the work of [19]. In the loading step, voltages are set such that the fluid flows from top to bottom (N-S) in the vertical channels and toward the intersection in the horizontal channels. In the sample injection step, the applied voltages are instantaneously switched (W at the highest voltage, N, S at high, E at ground), and the sample is injected in the horizontal channel under an applied electric field of 16kV/m. During the sample injection step, fluid flows from left to right in the horizontal channel and away from the intersection in the vertical channels [20]. Between injections, the channel is flushed using the same scheme as the loading step.

A.2 Fluorescence Imaging:

The transport and spatial distribution of fluorescent analytes were imaged with an inverted epifluorescence microscope (Olympus IX70, Olympus, Inc.) fitted with a 60X water immersion objective lens (1.0 NA, Olympus, Inc.) and a 0.5X lens tube, to increase sensitivity. Illumination from a 200 W Hg-arc lamp was filtered with a FITC fluorescence filter cube (Omega, Inc.) containing excitation and emission filters and a dichroic mirror matched to the fluorescence spectrum of 6-FAM. Images were recorded using a back illuminated EMCCD camera (Ixon Ultra897, Andor Technology) with a 512 x 512 pixel array and 16-bit digitization to a PC [21]. Frame rate (10 to 20 Hz) and exposure time (0.05 to 0.1 s) varied depending on the channel depth and analyte. Background subtraction was performed on all images using custom Matlab (The MathWorks) programs, to enhance signal to noise ratio [21].

A.2 Microfluidic Electrophoretic Mobility Measurements:

The electrophoretic mobility was determined directly from elution time measurements during electrokinetic injections, as described by Pennathur, et al. [20]. Briefly, the microscope objective was positioned downstream of the injection point, and the velocity, v_{meas} , was computed as the ratio of distance from injection, L , and the measured time, t , required for the analyte to reach the center of the field of view (see Figure 13). The ζ potential needed to compute v_{EOF} from the Helmholtz-Smoluchowski equation [22] was found for each experiment from the velocity measurement of a fluorescein marker that was injected with the DNA sample. The electrophoretic mobility of fluorescein was determined in a separate set of experiments [23]. Although the calculation of the electroosmotic velocity v_{EOF} is trivial for microchannels, to find the correct electroosmotic flow in nanochannels we numerically solved the non-linear Poisson-Boltzmann equation, and used the mean of the resultant velocity profile [24]. Once v_{EOF} was determined, it was subtracted from the measured velocity to give the electrophoretic velocity of the analyte, v_{EP} . Finally, to determine electrophoretic mobility, μ_{EP} , the electrophoretic velocity v_{EP} was divided by the electric field E :

$$\mu_{EP} = \frac{1}{E} v_{EP} = \frac{1}{E} (v_{meas} - v_{EOF}) = \frac{1}{E} \left(\frac{L}{t} - v_{EOF} \right) \quad (1)$$

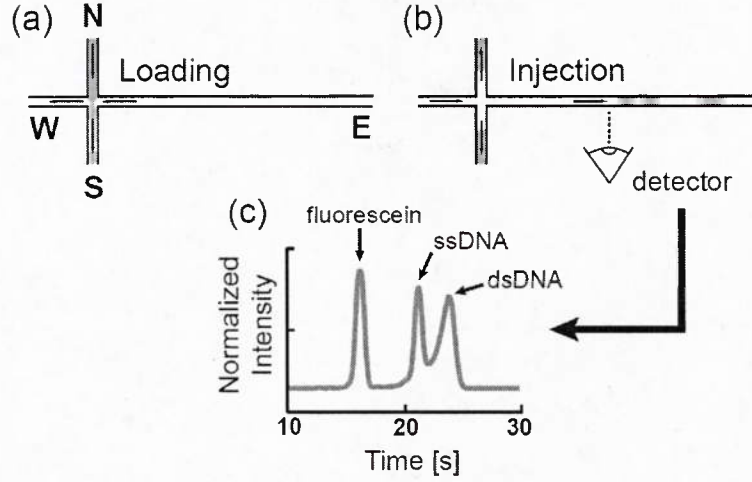


Figure 13: Schematic of sample injection and separation within a nanofluidic platform, as well as an example of a typical electropherogram obtained in our study. After loading (a), the sample is injected along the horizontal channel (b). A detector senses the arrival of the sample as a variation in the measured background signal, generating an electropherogram. The characteristic electropherogram shown here (c) demonstrates the separation of 10 bp ss- (peak 2) and dsDNA (peak 3) in a 1 μm deep channel; fluorescein (peak 1), is a mobility marker.

A.2 Experimental Results And Discussion

Figure 14 shows the electropherograms of 10, 20, 50 bp ss- and dsDNA in a 1 μm channel at buffer ionic strengths of 10, 15, 20, 30 and 60 mM. In each plot, the time axis is scaled to ease comparisons, according to the following formula:

$$t_{\text{scaled},XmM} = t_{\text{meas},XmM} \frac{t_{FL,10mM}}{t_{FL,XmM}} \quad (2)$$

where $t_{\text{meas},XmM}$ is the time measured at ionic strength XmM (i.e., current experiment), $t_{FL,10mM}$ and $t_{FL,XmM}$ are the fluorescein arrival times at, respectively, 10mM and XmM . Scaling compensates for the longer detection times at higher ionic strengths, which have lower channel ζ potentials and therefore slower electroosmotic flow [29], thus allowing for comparison across all experimental conditions. We note that some electropherograms show more than the expected three peaks (i.e., fluorescein, ssDNA, dsDNA): we attribute them to populations of fragmented DNA, resulting from the DNA synthesis, and often observed in DNA separation experiments under similar conditions [5], [30].

DNA behavior and separation dynamics are affected by a number of coupled physical mechanisms, including (i) hydrodynamic interactions, (ii) salt-dependent EDL changes around the DNA, which alter its size/conformation, (iii) differences in drag due to length dependent conformational differences, (iv) confinement effects due to shrinking channel size, and (v) electrostatic repulsion from walls. The result is a highly complex system, where each parameter needs to be carefully designed in order to maximize separation resolution. Figure 14 shows some interesting general trends. First, we note that, for any strand length, the peak separation resolution increases with ionic strength. For longer strands, this effect can be attributed in part to the longer arrival time to the detector. In addition, at higher ionic strengths, the 50 base ssDNA

conformation will be more compact, thereby reducing the drag and lowering the absolute electrophoretic mobility (i.e., allowing for the DNA to elute faster).

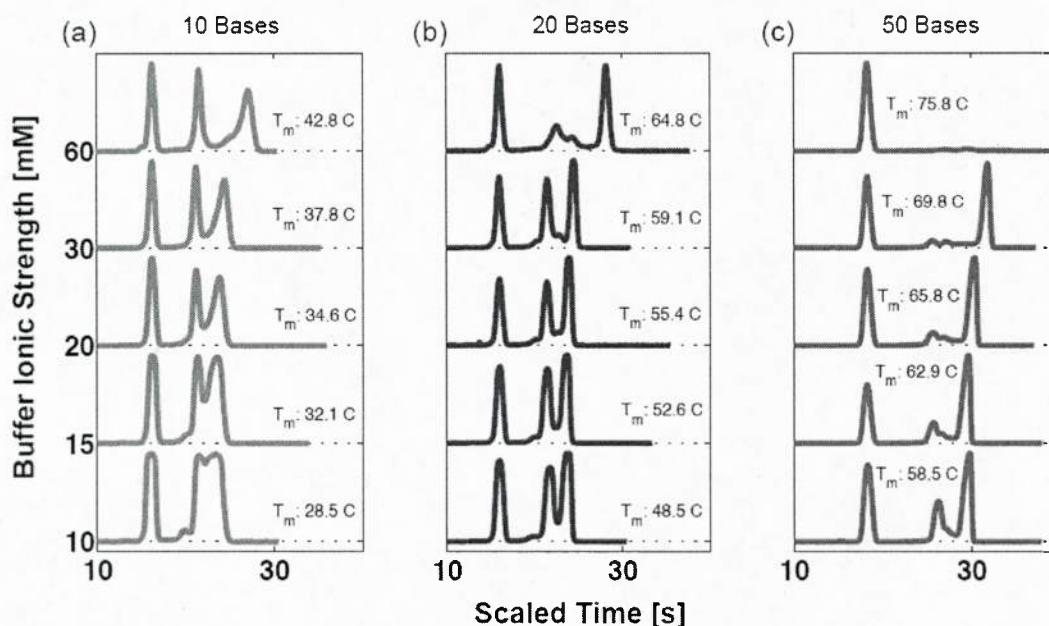


Figure 14: Scaled electropherograms of all ss- and dsDNA experiments in a 1 μm channel. Electropherograms are scaled due to the large ionic strength based changes in electroosmotic mobility. The scaling aligns the fluorescein peaks to show the change in resolution as a function of ionic strength. Melting temperatures, T_m , for DNA at each condition are superposed on the electropherograms. Each electropherogram is plotted as an average of raw data trials.

Figure 14 also shows low separation resolution of the 10 bp strands at low ionic strength. This is a consequence of hybridization interactions (effect (i)), because and the melting temperature, T_m (and therefore K_D , the dissociation constant that describes the equilibrium ratio of ds- to ssDNA), is close to room temperature. As a result, during the experiments, the short complementary DNA are in a dynamic equilibrium, continuously associating and disassociating, with significant impact on the separation resolution. To better understand this dynamic, we computed equilibrium ratios using the DINAmelt webserver, given DNA concentrations, sequence, and ionic strengths. From these values, we determined initial K_D 's. Note that, due to the non-equilibrium nature of our injection experiments, equilibrium ratios are constantly changing during experiments. For example, the equilibrium ratio of ss- to dsDNA for 10 base in 10mM buffer is initially 0.0474, when there is an excess of primary ssDNA present. However, the ratio can increase to 0.1747, after the excess ssDNA separates from the rest of the plug. Diffusion and dispersion of the sample lower the concentration further, increasing the equilibrium ratio even more. On Figure 14, we write the range of T_m calculated from DINAmelt for the equilibrium ratio at the start of the experiment (higher T_m) and during the experiment (lower T_m). For a more detailed discussion on the effect of kinetics on such separations, we refer the reader to [31].

Finally, we note the extremely low signal corresponding to the 50 bp single strand, which decreases even further at higher ionic strengths. A similar effect can be seen also for the 20 bp peak at the highest buffer ionic strength. We hypothesize this phenomenon is a consequence of using a FAM tag with our specific guanine (G) rich DNA sequence, which has been shown to efficiently quench fluorescence [32]. Longer ssDNA in high ionic strength solutions can assume

more compact structures, owing to their flexibility and screening of electrostatic repulsion between monomers. The result is an increase in the amount of G near the 6-FAM that contributes to quenching. Furthermore, since the 50 base strand is made of 5 repeats of the 10 base G-rich strand, there is high probability for G-quadruplex formation [33] or other offset hybridization configurations, which could enhance fluorescence quenching or affect the solubility of the ssDNA. This effect is reduced upon hybridization to the complementary strand to form stiff, rod-like dsDNA, which moves many of the G away from the 6-FAM tag at the 5' end of the DNA. Fluorescence measurements (not reported here) of the 6-FAM tagged ss- and dsDNA, performed in a well plate using a Tecan Infinite 200Pro, confirmed a ~50% decrease in the fluorescence of the ssDNA compared to the dsDNA.

The complete set of measured values for the electrophoretic mobilities of ss- and dsDNA in 100 nm and 1 μ m channels is shown in Figure 15, as well as listed in Table 1.

Table 1: Absolute electrophoretic mobilities and associated errors for all the ss- and dsDNA measured in 1 μ m and 100 nm deep microfluidic channels. Errors represent 95% confidence intervals according to the number of trials listed in Table 1.

Absolute Electrophoretic Mobility [E-8 m ² /Vs]						
			10mM	15mM	20mM	30mM
1 μ m	10	ss	3.90 \pm 0.02	3.70 \pm 0.01	3.55 \pm 0.01	3.37 \pm 0.02
		ds	4.12 \pm 0.04	3.95 \pm 0.03	3.82 \pm 0.01	3.65 \pm 0.01
	20	ss	3.95 \pm 0.03	3.75 \pm 0.03	3.61 \pm 0.01	3.44 \pm 0.01
		ds	4.19 \pm 0.03	3.99 \pm 0.02	3.86 \pm 0.00	3.69 \pm 0.01
	50	ss	3.96 \pm 0.01	3.78 \pm 0.01	3.64 \pm 0.01	3.45 \pm 0.01
		ds	4.24 \pm 0.01	4.08 \pm 0.01	3.95 \pm 0.00	3.79 \pm 0.02
100nm	10	ss	3.64 \pm 0.03	3.52 \pm 0.02	3.40 \pm 0.01	3.24 \pm 0.01
		ds	3.81 \pm 0.04	3.72 \pm 0.02	3.61 \pm 0.01	3.51 \pm 0.02
	20	ss	3.68 \pm 0.00	3.59 \pm 0.03	3.46 \pm 0.06	3.29 \pm 0.01
		ds	3.92 \pm 0.04	3.84 \pm 0.01	3.72 \pm 0.00	3.56 \pm 0.01
	50	ss	3.64 \pm 0.03	3.52 \pm 0.02	3.40 \pm 0.01	3.24 \pm 0.01
		ds	3.81 \pm 0.04	3.72 \pm 0.02	3.61 \pm 0.01	3.51 \pm 0.02

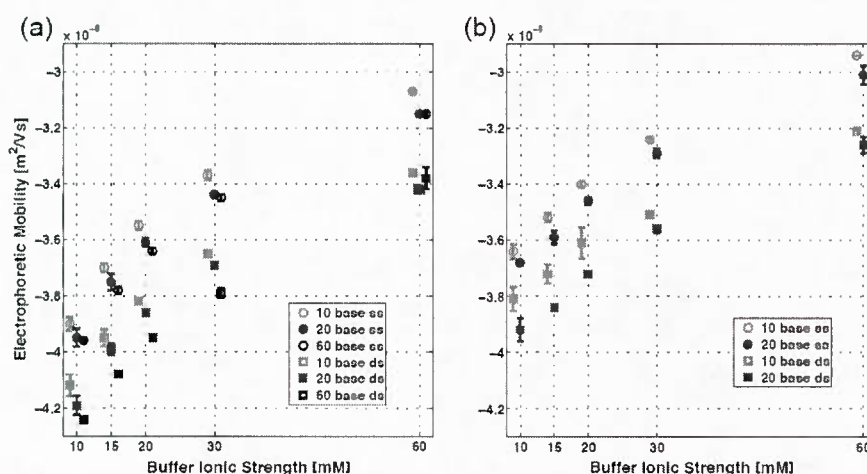


Figure 15: Electrophoretic mobility of 10, 20 and 50 ss- and dsDNA measured in: a) 1 μ m and b) 100 nm deep channels. Data points corresponding to the same ionic strength have been plotted slightly apart (in

the x direction) for the ease of the reader. Error bars correspond to the standard deviation of all trials for a given experiment.

In all cases, as the ionic strength increases, the absolute electrophoretic mobilities decrease, which we attribute to the charged solvent effect and asymmetry field proposed by Manning, and experimentally confirmed for short DNA oligomers (effect (ii)) [17], [26], [34]. In all cases, ssDNA absolute electrophoretic mobilities are smaller than dsDNA, presumably because dsDNA has a higher charge density [18]. It is also interesting to note that recent work by Stellwagen and Stellwagen, using capillary electrophoresis, showed that the separation resolution between ssDNA and dsDNA was inadequate in the range of 10-20 base lengths, and that 10 base ssDNA actually had a higher electrophoretic mobility than 10 bp dsDNA [35]. Their experiments were performed in 0.5-2kV/m applied electric fields, with a detection point 29.8 cm downstream. Conversely, our experiments were performed in much shallower channels ($\leq 1\mu\text{m}$), which allowed us to apply $\sim 8\times$ larger electric field strengths without significant Joule heating, and thus detect at shorter distances (1 cm). This fact, combined with shorter injection plug lengths, allows us to minimize diffusion effects and greatly increase separation resolution.

To further understand the mechanisms involved in DNA separation, we investigate the electrophoretic mobility difference between ss- and dsDNA versus buffer ionic strength and strand length, shown in Figure 16, in both $1\mu\text{m}$ and 100 nm channels. The dominant parameter in determining the difference in electrophoretic mobility between ss- and dsDNA is the shape of DNA, which is affected by salt-dependent EDL changes around the DNA, and results in differences in drag (effect (iii)). The DNA shape is related to its persistence length, L_p , which for dsDNA ($\sim 45\text{-}50\text{ nm}$) is larger than the contour length of any of the strands used in this study, for all ionic strengths considered [36]. Therefore, in this study only ssDNA will exhibit conformational changes that may affect electrophoretic mobility. However, for the 10 and 20 base ssDNA, the changes in L_p are too small to induce any appreciable change in conformation: indeed, we see that in Figure 16 the difference in mobility for the 20 bp strands remains approximately constant. Instead, we believe that the downward trend we see in Figure 16 for 50 base strands, is most likely due to these conformational changes. When ionic strength ranges from 10 to 60 mM, the ratio of strand length to persistence length of the 50 base ssDNA increases from 8.2 to 9.9 (whereas it is only a shift from 3.3 to 4 for 20 base ssDNA, and 1.6 to 2 for 10 base ssDNA). These ratios correspond to a 46% and 43% mean end-to-end difference for the 10 mM case and 60 mM case respectively [37], [38]. Thus, we conclude that as the ionic strength increases, the 50 base ssDNA tends to assume a more compact shape, which induces a significant increase in drag and results in a higher electrophoretic mobility, and consequently, in the downward trend observed in Figure 15.

For 10 bp DNA, we hypothesize that the mobility trend is due to reaction kinetics within the dsDNA peak. In general, the observed electrophoretic mobility of dsDNA is dependent on the equilibrium ratio of ss- to dsDNA: when the equilibrium ratio is large, the dsDNA peak is composed of mostly ssDNA and, thus, migrates with an electrophoretic mobility that is closer to the electrophoretic mobility of ssDNA. For example, in 10 mM buffer the melting temperature ($T_m=32.1^\circ\text{C}$) is closest to room temperature and, therefore, has the highest equilibrium ratio of all conditions. In this case, the observed dsDNA electrophoretic mobility is closest to the ssDNA value, and results in poor separation resolution (Figure 14a, lower trace). As T_m increases (which happens as the ionic strength increases), the equilibrium ratio decreases: separation resolution improves, as the dsDNA peak migrates further away from the ssDNA, and its

electrophoretic mobility gets closer to its true value (i.e., the value when dsDNA does not disassociate). Instead, for 20 and 50 base DNA, at all ionic strengths, T_m is sufficiently high to result in extremely low equilibrium ratios, which thus have negligible effects on transport. Note that, as the DNA elutes down the separation channel, the equilibrium ratios constantly change due to separation dynamics, and therefore, the calculated melting temperatures are only approximate.

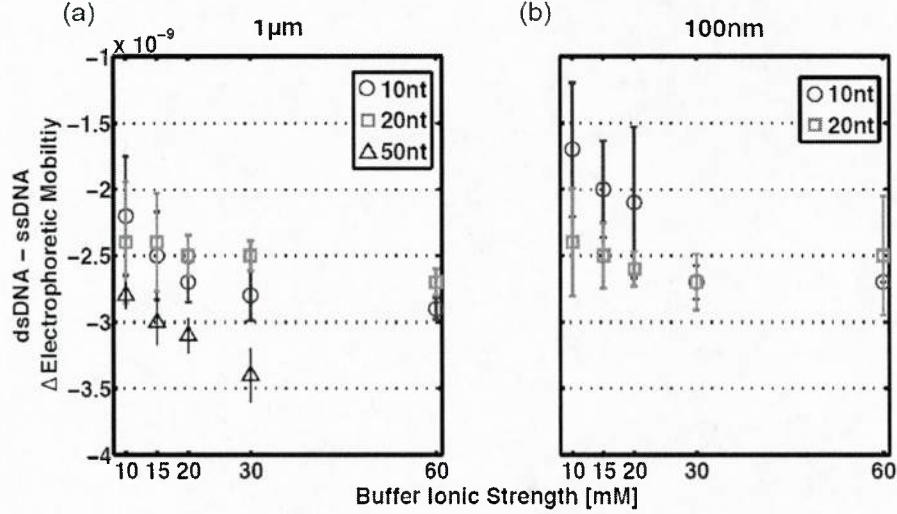


Figure 16: Difference of electrophoretic mobility between ss- and dsDNA for 10, 20, and 50 bp DNA in both 1 μm (a) and 100 nm (b) channels. Data shows a downward trend for the 10 and 50 bp (due to changes in melting temperature and persistence length respectively), and no change for the 20 bp case. Error bars correspond to the standard deviation of all trials for a given experiment.

In Figure 17, we investigate the effect of hydrodynamic confinement (effect (iv)) more closely by plotting the percent reduction in electrophoretic mobility between a 1 μm and 100 nm deep channels. First, we notice that the behavior of ss- and dsDNA is qualitatively very similar. This suggests that, at least for DNA smaller than 20 bp, confinement into nanometer sized channels affects ss- and dsDNA mobility in the same way. Furthermore, in all cases, the mobility at higher salt is reduced by about 4%. We attribute this reduction to an increase in drag due to hydrodynamic confinement.

To support this hypothesis, we analytically solve for the drag on a spherical particle flowing between two walls, using the analytical expression below [39]:

$$D_{\parallel} = D_0 \left(1 - \frac{9}{16} \left[\left(\frac{a}{z} \right) + \left(\frac{a}{(h-z)} \right) \right] + \frac{1}{8} \left[\left(\frac{a}{z} \right)^3 + \left(\frac{a}{(h-z)} \right)^3 \right] - \frac{45}{256} \left[\left(\frac{a}{z} \right)^4 + \left(\frac{a}{(h-z)} \right)^4 \right] - \frac{1}{16} \left[\left(\frac{a}{z} \right)^5 + \left(\frac{a}{(h-z)} \right)^5 \right] \right) \quad (3)$$

where a is the sphere radius, h is the channel height, z is the distance from the center of the sphere to the wall, and D_0 is the free solution diffusivity.

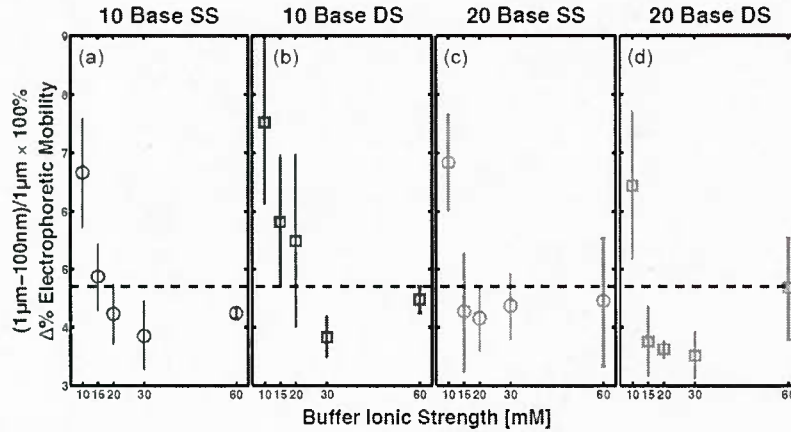


Figure 17: Percent difference in electrophoretic mobility between 1 μm and 100 nm channels for 10 and 20 bp ss- and dsDNA for different salt concentrations. Dashed horizontal line represents the expected, theoretically derived, reduction in electrophoretic mobility due to increases in hydrodynamic interactions with the wall only in 100nm channels. The larger differences in mobility at low ionic strengths are due to electric double layer interactions between the walls and the DNA. Error bars correspond to the standard deviation of all trials for a given experiment.

For ssDNA, we approximate a as being equal to the DNA persistence length. This way, we find that the hydrodynamic drag increase for ssDNA, going from 1 μm to 100nm channel, is about 4.8% (ssDNA persistence length is 2.02 nm at 60mM [39]), which is in good agreement with our data. For dsDNA, the spherical approximation is geometrically inaccurate, as these strands will tend to retain a rod-like shape at all salt concentrations studied here. At the same time, the rigid cylinder approximation fails to give meaningful estimates of the drag coefficient, because it assumes a larger aspect ratio than DNA's.

Figure 17 also shows a general decreasing trend in the electrophoretic mobility difference between 1 μm and 100 nm channels as the buffer ionic strength increases, coming to a plateau at larger ionic strengths. As ionic strength increases, the characteristic size of the EDL or the Debye length, λ_D , decreases from 1.70 nm at 10mM, to 1.03 nm at 60mM, and any electrostatic interactions between the walls and DNA become negligible, regardless of channel height. At the lowest ionic strength, the EDL accounts for 3.4% of the channel height for the 100nm deep channel compared to 0.34% of the 1 μm deep channel. We, therefore, hypothesize that the increase in electrophoretic mobility difference between DNA in different channel heights at low salt concentration is due to electrostatic interactions between the DNA and the EDL (effect (v)) that cause particles to move towards the center of the channel, where the fluid velocity is greatest [25]. This reduces the time to arrival at the detector (because electroosmotic flow is larger than electrophoretic in our experiments), making the calculated electrophoretic mobility smaller (see Equation 1). Based on [25], the differences in overall velocity attributed to the EDL interactions for a particle with order -1 charge would be on the order of one percentage, and would quickly become negligible as λ_D/h decreases. Thus, we believe that the predominant cause for the difference between the mobilities of DNA in the 1 μm and 100nm channels is likely due to such drag effects. A full theoretical/numerical development of the EDL effects on both the DNA and the wall is beyond the scope of this paper, which primarily focuses on experimental measurements with heuristic arguments meant to support plausible hypothesis explaining our findings. In future work, we will pursue more detailed theoretical modeling, which so far we have developed only for the simplified case of spherical particles.

A.2 Conclusions:

Our results show that identification of short (10, 20, and 50 bases long) DNA strands using nanofluidic channels is possible. Although the initial work plan included the investigation of DNA separation and identification under different sample conditions (non or partially complementary strands), early on our data highlighted the complexity of DNA separations in channels, and the various effects that can change the observed behavior. Therefore, in consultation with Dr. King, it was decided that investigating the fundamental science underlying the dynamics of DNA in micro and nanoconfinements should be pursued first, as a prerequisite to engineering optimal separation platforms.

What we found is that buffer ionic strength is the largest factor affecting the electrophoretic mobility of DNA, but we also showed that DNA length, conformation, and confinement are important variables. Specifically, we showed that for short (10bp) ss- and dsDNA, one needs to consider the impact of melting temperature on strand mobility and separation resolution; while for longer strands (50bp), conformation effects play an important role in determining mobility. Finally, we showed the effects of confinement on the absolute electrophoretic mobility of 10 and 20bp ss- and dsDNA, and are able to isolate the effects of hydrodynamic confinement and EDL interactions. These results are the basis for further investigations to increase the sensitivity and resolution of DNA separations, as well as for understanding the kinetics of DNA with low melting temperatures. Future steps will include further improving a COMSOL model that we started to develop to compare experimental results with theory, and that will prove especially useful in understanding the coupling between separation efficiency and DNA hybridization dynamics.

References

- [1] Sustarich, J. M., Storey, B. D. and Pennathur, S., *Field amplified sample stacking and focusing in nanofluidic channels*, Physics of Fluids, 2010, 22, p. 112003.
- [2] N. J. Schork, D. Fallin, and J. S. Lanchbury, "Single nucleotide polymorphisms and the future of genetic epidemiology.," *Clinical genetics*, vol. 58, no. 4, pp. 250–64, Oct. 2000.
- [3] J.-B. Fan, M. S. Chee, and K. L. Gunderson, "Highly parallel genomic assays.," *Nature reviews. Genetics*, vol. 7, no. 8, pp. 632–44, Aug. 2006.
- [4] D. R. Call, "Challenges and opportunities for pathogen detection using DNA microarrays.," *Critical reviews in microbiology*, vol. 31, no. 2, pp. 91–9, Jan. 2005.
- [5] S. Pennathur, F. Baldessari, J. G. Santiago, M. G. Kattah, J. B. Steinman, and P. J. Utz, "Free-Solution Oligonucleotide Separation in Nanoscale Channels," *Anal. Chem*, vol. 79, no. 21, pp. 8316–8322, 2007.
- [6] P. J. Atzberger, P. R. Kramer, and C. S. Peskin, "A stochastic immersed boundary method for fluid-structure dynamics at microscopic length scales," *Journal of Computational Physics*, vol. 224, no. 2, pp. 1255–1292, 2007.
- [7] J. D. Cross, E. A. Strychalski, and H. G. Craighead, "Size-dependent {DNA} mobility in nanochannels," *J. Appl. Phys.*, vol. 102, no. 2, p. 24701, 2007.

- [8] J. T. Mannion, C. H. Reccius, J. D. Cross, and H. G. Craighead, "Conformational Analysis of Single DNA Molecules Undergoing Entropically Induced Motion in Nanochannels," *Biophysical Journal*, vol. 90, no. 12, pp. 4538–4545, 2006.
- [9] F. Tessier, J. Labrie, and G. W. Slater, "Electrophoretic separation of long polyelectrolytes in submolecular-size constrictions: a Monte Carlo study," *Macromolecules*, vol. 35, no. 12, pp. 4791–4800, 2002.
- [10] A. S. Panwar and S. Kumar, "Time Scales in Polymer Electrophoresis through Narrow Constrictions: A Brownian Dynamics Study," *Macromolecules*, vol. 39, no. 3, pp. 1279–1289, Feb. 2006.
- [11] J. Han, S. Turner, and H. Craighead, "Entropic Trapping and Escape of Long DNA Molecules at Submicron Size Constriction," *Physical Review Letters*, vol. 83, no. 8, pp. 1688–1691, Aug. 1999.
- [12] J. Han and H. G. Craighead, "Separation of Long {DNA} Molecules in a Microfabricated Entropic Trap Array," *Science*, vol. 288, no. 5468, pp. 1026–1029, 2000.
- [13] J. Han and H. G. Craighead, "Characterization and Optimization of an Entropic Trap for {DNA} Separation," *Anal. Chem.*, vol. 74, no. 2, pp. 394–401, 2002.
- [14] R. M. Levy and E. Gallicchio, "Computer simulations with explicit solvent: recent progress in the thermodynamic decomposition of free energies and in modeling electrostatic effects.," *Annual review of physical chemistry*, vol. 49, pp. 531–67, Jan. 1998.
- [15] M. K. Gilson and H.-X. Zhou, "Calculation of protein-ligand binding affinities.," *Annual review of biophysics and biomolecular structure*, vol. 36, pp. 21–42, Jan. 2007.
- [16] G. S. Manning, "Limiting Laws and Counterion Condensation in Polyelectrolyte Solutions , 7 . Electrophoretic Mobility and Conductance," *Journal of Physical Chemistry*, vol. 185, no. 4, pp. 1506–1515, 1981.
- [17] E. Stellwagen and N. C. Stellwagen, "The free solution mobility of DNA in Tris-acetate-EDTA buffers of different concentrations, with and without added NaCl.," *Electrophoresis*, vol. 23, no. 12, pp. 1935–41, Jun. 2002.
- [18] N. C. Stellwagen, C. Gelfi, and P. G. Righetti, "The Free Solution Mobility of DNA," *Biopolymers*, vol. 42, pp. 687–703, 1997.
- [19] S. Pennathur and J. G. Santiago, "Electrokinetic Transport in Nanochannels. 2. Experiments," *Analytical Chemistry*, vol. 77, no. 21, pp. 6782–6789, 2005.
- [20] T. Driehorst, P. O'Neill, P. M. Goodwin, S. Pennathur, and D. K. Fygenson, "Distinct conformations of DNA-stabilized fluorescent silver nanoclusters revealed by electrophoretic mobility and diffusivity measurements.," *Langmuir : the ACS journal of surfaces and colloids*, vol. 27, no. 14, pp. 8923–33, Jul. 2011.
- [21] N. R. Markham and M. Zuker, "DINAMelt web server for nucleic acid melting prediction.," *Nucleic Acids Research*, vol. 33, pp. W577–W581, 2005.

- [22] N. R. Markham and M. Zuker, *Bioinformatics : Structure, Function and Applications*, Methods in. Springer, 2008, pp. 3–31.
- [23] R. Bharadwaj, J. G. Santiago, and B. Mohammadi, “Design and optimization of on-chip capillary electrophoresis,” *Electrophoresis*, vol. 23, no. 16, pp. 2729–2744, 2002.
- [24] M. Napoli, P. Atzberger, and S. Pennathur, “Experimental study of the separation behavior of nanoparticles in micro- and nanochannels,” *Microfluidics and Nanofluidics*, vol. 10, no. 1, pp. 69–80, 2011.
- [25] S. Pennathur and J. G. Santiago, “Electrokinetic Transport in Nanochannels. 1. Theory,” *Analytical Chemistry*, vol. 77, no. 21, pp. 6772–6781, 2005.
- [26] Q. Dong, E. Stellwagen, J. M. Dagle, and N. C. Stellwagen, “Free solution mobility of small single-stranded oligonucleotides with variable charge densities,” *Electrophoresis*, vol. 24, no. 19–20, pp. 3323–9, Oct. 2003.
- [27] E. Stellwagen and N. C. Stellwagen, “Determining the electrophoretic mobility and translational diffusion coefficients of DNA molecules in free solution,” *Electrophoresis*, vol. 23, no. 16, pp. 2794–803, Aug. 2002.
- [28] J. Fu, P. Mao, and J. Han, “Nanofilter array chip for fast gel-free biomolecule separation,” *Appl. Phys. Lett.*, vol. 87, no. 26, p. 263902, 2005.
- [29] B. J. Kirby, *Micro- and Nanoscale Fluid Mechanics: Transport in Microfluidic Devices*. Cambridge Univ Press, 2009.
- [30] N. C. Stellwagen, S. Magnusdottir, C. Gelfi, and P. G. Righetti, “Preferential counterion binding to A-tract DNA oligomers,” *Journal of molecular biology*, vol. 305, no. 5, pp. 1025–33, Feb. 2001.
- [31] T. M. Wynne and S. Pennathur, “Analysis of non-equilibrium analyte kinetics during capillary electrophoresis,” *submitted to Analytical Chemistry*, 2013.
- [32] M. Torimura, S. Kurata, and K. Yamada, “Fluorescence-quenching phenomenon by photoinduced electron transfer between a fluorescent dye and a nucleotide base,” *Analytical sciences*, 2001.
- [33] S. Burge, G. N. Parkinson, P. Hazel, A. K. Todd, and S. Neidle, “Quadruplex DNA: sequence, topology and structure,” *Nucleic acids research*, vol. 34, no. 19, pp. 5402–15, Jan. 2006.
- [34] G. S. Manning, “Limiting laws and counterion condensation in polyelectrolyte solutions. 7. Electrophoretic mobility and conductance,” *The Journal of Physical Chemistry*, vol. 85, no. 11, pp. 1506–1515, May 1981.
- [35] E. Stellwagen, Y. Lu, and N. C. Stellwagen, “Unified Description of Electrophoresis and Diffusion for DNA and Other Polyions,” *Biochemistry*, vol. 42, pp. 11745–11750, 2003.
- [36] Y. Lu, B. Weers, and N. C. Stellwagen, “DNA persistence length revisited,” *Biopolymers*, vol. 61, no. 4, pp. 261–275, 2002.

- [37] M. Mandelkern, J. Elias, D. Eden, and D. Crothers, "The dimensions of DNA in solution," *Journal of Molecular Biology*, vol. 152, p. 153, 1981.
- [38] J. Howard, *Mechanics of Motor Proteins and the Cytoskeleton*. Sinauer Associates, Inc., MA, 2001.
- [39] T. M. Wynne, A. H. Dixon, and S. Pennathur, "Electrokinetic characterization of individual nanoparticles in nanofluidic channels," *Microfluidics and Nanofluidics*, vol. 12, no. 1–4, pp. 411–421, Sep. 2011.

REPORT OF INVENTIONS AND SUBCONTRACTS (Pursuant to "Patent Rights" Contract Clause) (See Instructions on back)							Form Approved OMB No. 9000-0095 Expires Jan 31, 2008		
<p>The public reporting burden for this collection of information is estimated to average 1 hour per response, including the time for reviewing instructions, searching existing data sources, gathering and maintaining the data needed, and completing and reviewing the collection of information. Send comments regarding this burden estimate or any other aspect of this collection of information, including suggestions for reducing the burden, to the Department of Defense, Executive Services Directorate (9000-0095). Respondents should be aware that notwithstanding any other provision of law, no person shall be subject to any penalty for failing to comply with a collection of information if it does not display a currently valid OMB control number.</p> <p>PLEASE DO NOT RETURN YOUR COMPLETED FORM TO THE ABOVE ORGANIZATION. RETURN COMPLETED FORM TO THE CONTRACTING OFFICER.</p>									
1.a. NAME OF CONTRACTOR/SUBCONTRACTOR		c. CONTRACT NUMBER		2.a. NAME OF GOVERNMENT PRIME CONTRACTOR		c. CONTRACT NUMBER		3. TYPE OF REPORT (X one)	
				The Regents of the University of California		W9132T-12-2-0023		<input type="checkbox"/> INTERIM <input checked="" type="checkbox"/> b. FINAL	
b. ADDRESS (Include ZIP Code)		d. AWARD DATE (YYYYMMDD)		b. ADDRESS (Include ZIP Code)		d. AWARD DATE (YYYYMMDD)		4. REPORTING PERIOD (YYYYMMDD)	
				University of California, 3227 Chocoma Hall Santa Barbara, CA 93106		20120501		a. FROM 20120501 b. TO 20130630	
SECTION I - SUBJECT INVENTIONS									
5. "SUBJECT INVENTIONS" REQUIRED TO BE REPORTED BY CONTRACTOR/SUBCONTRACTOR (If "None," so state)									
NAME(S) OF INVENTOR(S) (Last, First, Middle Initial)		TITLE OF INVENTION(S)		DISCLOSURE NUMBER, PATENT APPLICATION SERIAL NUMBER OR PATENT NUMBER		ELECTION TO FILE PATENT APPLICATIONS (X)		CONFIRMATORY INSTRUMENT OR ASSIGNMENT FORWARDED TO CONTRACTING OFFICER (X)	
e.		b.		c.		d.		e.	
						(1) UNITED STATES (2) FOREIGN (a) YES (b) NO (a) YES (b) NO		(a) YES (b) NO (a) YES (b) NO	
Pennathur, Sumita		None							
f. EMPLOYER OF INVENTOR(S) NOT EMPLOYED BY CONTRACTOR/SUBCONTRACTOR					g. ELECTED FOREIGN COUNTRIES IN WHICH A PATENT APPLICATION WILL BE FILED				
(1) (a) NAME OF INVENTOR (Last, First, Middle Initial)		(2) (a) NAME OF INVENTOR (Last, First, Middle Initial)		(1) TITLE OF INVENTION		(2) FOREIGN COUNTRIES OF PATENT APPLICATION			
(b) NAME OF EMPLOYER		(b) NAME OF EMPLOYER							
(c) ADDRESS OF EMPLOYER (Include ZIP Code)		(c) ADDRESS OF EMPLOYER (Include ZIP Code)							
SECTION II - SUBCONTRACTS (Containing a "Patent Rights" clause)									
6. SUBCONTRACTS AWARDED BY CONTRACTOR/SUBCONTRACTOR (If "None," so state)									
NAME OF SUBCONTRACTOR(S)		ADDRESS (Include ZIP Code)		SUBCONTRACT NUMBER(S)		FAR "PATENT RIGHTS"		DESCRIPTION OF WORK TO BE PERFORMED UNDER SUBCONTRACT(S)	
a.		b.		c.		d.		e.	
						(1) CLAUSE NUMBER (2) DATE (YYYYMM)			
SECTION III - CERTIFICATION									
7. CERTIFICATION OF REPORT BY CONTRACTOR/SUBCONTRACTOR (Not required if: (X) as appropriate)						<input type="checkbox"/> SMALL BUSINESS or <input checked="" type="checkbox"/> NONPROFIT ORGANIZATION			
I certify that the reporting party has procedures for prompt identification and timely disclosure of "Subject Inventions," that such procedures have been followed and that all "Subject Inventions" have been reported.									
a. NAME OF AUTHORIZED CONTRACTOR/SUBCONTRACTOR OFFICIAL (Last, First, Middle Initial)		b. TITLE		c. SIGNATURE				d. DATE SIGNED	

REPORT DOCUMENTATION PAGE			Form Approved OMB No. 0704-0188		
Public reporting burden for this collection of information is estimated to average 1 hour per response, including the time for reviewing instructions, searching existing data sources, gathering and maintaining the data needed, and completing and reviewing this collection of information. Send comments regarding this burden estimate or any other aspect of this collection of information, including suggestions for reducing this burden to Department of Defense, Washington Headquarters Services, Directorate for Information Operations and Reports (0704-0188), 1215 Jefferson Davis Highway, Suite 1204, Arlington, VA 22202-4302. Respondents should be aware that notwithstanding any other provision of law, no person shall be subject to any penalty for failing to comply with a collection of information if it does not display a currently valid OMB control number. PLEASE DO NOT RETURN YOUR FORM TO THE ABOVE ADDRESS.					
1. REPORT DATE (DD-MM-YYYY) 09-30-2013		2. REPORT TYPE Final technical		3. DATES COVERED (From - To) May 2012 - Jun 2013	
4. TITLE AND SUBTITLE Nanofluidic LaB-ON-Chip Technology for DNA Identification			5a. CONTRACT NUMBER		
			5b. GRANT NUMBER W9132T-12-2-0023		
			5c. PROGRAM ELEMENT NUMBER		
6. AUTHOR(S) Sumita Pennathur			5d. PROJECT NUMBER		
			5e. TASK NUMBER		
			5f. WORK UNIT NUMBER		
7. PERFORMING ORGANIZATION NAME(S) AND ADDRESS(ES) Office of Research University of California 3227 Cheadle Hall, 3rd floor Santa Barbara, CA 93106-2050			8. PERFORMING ORGANIZATION REPORT NUMBER		
9. SPONSORING / MONITORING AGENCY NAME(S) AND ADDRESS(ES) ERDC-CERL ATTN: CECER-CN-E P.O. Box 9005 Champaign, IL 61826-9005			10. SPONSOR/MONITOR'S ACRONYM(S) ERDC-CERL		
			11. SPONSOR/MONITOR'S REPORT NUMBER(S)		
12. DISTRIBUTION / AVAILABILITY STATEMENT Publicly available.					
13. SUPPLEMENTARY NOTES					
14. ABSTRACT In this project we have investigated the potential of nanofluidic lab-on-chip technology to be used as platforms for free-flow separation, concentration, and identification of biomolecules. Specifically, the goals of this project have been to: 1) demonstrate Field Amplified Sample Stacking (FASS) for specific DNA samples, and 2) demonstrate identification of target single stranded DNA (ssDNA) from a complex mixture of DNA, containing strands of different composition and size. We have achieved both goals and, in some cases, expanded the investigation from the original tasks. The results of our studies, elaborated in the following sections, suggest that lab-on-chip nanofluidic platforms may enable rapid and inexpensive, characterization and analysis of DNA biomarkers. Advantages include overall ease of operation of the device, which does not require loading of gels as sieving matrices; inexpensive analysis, as the only reagents required are water-based buffers; fast identification, since sample signatures can be produced in the order of less than a minute. Findings from this work have resulted in peer-reviewed publications (one conference and one journal paper). Potential target applications of our identification platform include analysis of DNA biomarkers for environmental pollutants or early disease diagnosis; analysis of mitochondrial DNA for forensic identification; investigation of protein kinetics.					
15. SUBJECT TERMS DNA separations, nanofluidics, microfluidic capillary electrophoresis (MCE), electrophoretic mobility, FASS, DNA concentration					
16. SECURITY CLASSIFICATION OF:			17. LIMITATION OF ABSTRACT UU	18. NUMBER OF PAGES	19a. NAME OF RESPONSIBLE PERSON Sumita Pennathur
a. REPORT UU	b. ABSTRACT UU	c. THIS PAGE UU			19b. TELEPHONE NUMBER (include area code) (805) 893-5510